

## Controlled bond expansion for DMRG ground state search at single-site costs

Andreas Gleis,<sup>1</sup> Jheng-Wei Li,<sup>1</sup> and Jan von Delft<sup>1</sup>

<sup>1</sup>Arnold Sommerfeld Center for Theoretical Physics, Center for NanoScience, and Munich Center for Quantum Science and Technology, Ludwig-Maximilians-Universität München, 80333 Munich, Germany

(Dated: August 1, 2022)

DMRG ground state search algorithms employing symmetries must be able to expand virtual bond spaces by adding or changing symmetry sectors if these lower the energy. Traditional single-site DMRG does not allow bond expansion; two-site DMRG does, but at much higher computational costs. We present a controlled bond expansion (CBE) algorithm that yields two-site accuracy and convergence per sweep, at single-site costs. Given a matrix product state  $\Psi$  defining a variational space, CBE identifies parts of the orthogonal space carrying significant weight in  $H\Psi$  and expands bonds to include only these. CBE-DMRG uses no mixing parameters and is fully variational.

DOI:

*Introduction.*— A powerful tool for studying ground state properties of one- and two-dimensional quantum systems is the density matrix renormalization group (DMRG) [1–7]. Prominent two-dimensional applications include the  $t$ - $J$  [8–11] and Hubbard [12–18] models, and quantum magnets [19–22]. Due to their high numerical costs, such studies are currently limited to either small finite-sized systems or cylinders with small circumference. Progress towards computationally cheaper DMRG ground state search algorithms would clearly be welcome.

In this paper, we address this challenge. A DMRG ground state search explores a variational space spanned by matrix product states. If symmetries are exploited, the algorithm must be able to expand the auxiliary spaces associated with virtual bonds by adjusting symmetry sectors if this lowers the energy. Traditional single-site or one-site (1s) DMRG, which variationally updates one site at a time, does not allow such bond expansions. As a result, it often gets stuck in metastable configurations having quantum numbers different from the actual ground state. Two-site (2s) DMRG naturally leads to bond expansion, but carries much higher computational costs.

Hence, schemes have been proposed for achieving bond expansions at sub-2s costs, such as density matrix perturbation [23] or subspace expansion [24]. However, in these schemes, the degree of subspace expansion per local update is controlled by a heuristic mixing factor. Depending on its value, some subspace expansion updates increase, rather than decrease, the energy.

Here, we present a controlled bond expansion (CBE) algorithm which lowers the energy with each step and yields 2s accuracy and convergence per sweep, at 1s costs. Given a matrix product state  $\Psi$  defining a variational space, our key idea is to identify parts of the 2s orthogonal space that carry significant weight in  $H\Psi$ , and to include only these parts when expanding the virtual bonds of a 1s Hamiltonian. Remarkably, these parts can be found via a projector that can be constructed at 1s costs.

*MPS basics.*— We briefly recall some standard MPS concepts [5], adopting the diagrammatic conventions of

Ref. 25. Consider an  $\mathcal{L}$ -site system with an open boundary MPS wavefunction  $\Psi$  having dimensions  $d$  for physical sites and  $D$  for virtual bonds.  $\Psi$  can be written in bond-canonical form w.r.t. to any bond  $\ell$ ,

The tensors  $\Lambda_\ell$  ( $\leftarrow$ ),  $A_\ell$  ( $\nabla$ ) and  $B_\ell$  ( $\nabla$ ) are variational parameters. They are linked by gauge relations,  $A_\ell \Lambda_\ell = \Lambda_{\ell-1} B_\ell$ , useful for shifting the bond tensor  $\Lambda_\ell$  to neighboring bonds.  $A_\ell$  and  $B_\ell$  are left and right-sided isometries, respectively, projecting  $Dd$ -dimensional *parent* ( $\text{P}$ ) spaces to  $D$ -dimensional *kept* ( $\kappa$ ) image spaces [25]; they satisfy

$$A_\ell^\dagger A_\ell = \begin{array}{c} A_\ell \\ \bigoplus \\ A_\ell^* \end{array} = \left( = \mathbb{1}_\ell^K, \quad B_\ell B_\ell^\dagger = \begin{array}{c} B_\ell \\ \bigoplus \\ B_\ell^* \end{array} = \right) = \mathbb{1}_{\ell-1}^K. \quad (2)$$

The Hamiltonian can similarly be expressed as a matrix product operator (MPO) with virtual bond dimension  $w$ ,

$$H = \star \square^{W_1} \square^{W_2} \cdots \square_d \square_w \square_d \cdots \square^{W_{\mathcal{L}-1}} \square^{W_{\mathcal{L}}} \quad (3)$$

For 2s or 1s DMRG, the energy of  $\Psi$  is lowered by projecting  $H$  to a local variational space associated with sites  $(\ell, \ell+1)$  or  $\ell$ , respectively, and using its ground state (GS) within that space to locally update  $\Psi$ . The corresponding 2s and 1s Hamiltonians can be computed recursively using

$$H_\ell^{1s} = \left[ \begin{array}{ccc|cc} & d & & & D \\ \ell-1 & \ell & \ell+1 & & \end{array} \right]^D = \left[ \begin{array}{ccccc|cc} & & & & & & & D \\ & \square & & \square & & & & \\ \ell-2 & \ell-1 & \ell & \ell+1 & & & & \\ & & & & & & & \end{array} \right] = \left[ \begin{array}{ccccc|cc} & & & & & & & \\ & \square & & \square & & & & \\ \ell-1 & \ell & \ell+1 & \ell+2 & & & & \end{array} \right]. \quad (4b)$$

To perform 2s or 1s updates, one replaces  $\psi_\ell^{2s} = A_\ell \Lambda_\ell B_{\ell+1}$  or  $\psi_\ell^{1s} = C_\ell = A_\ell \Lambda_\ell (\hat{\Phi})$  by the GS solutions of

$$(H_\ell^{2s} - E)\psi_\ell^{2s} = 0, \quad \text{Diagram} = E \frac{A_\ell \Lambda_\ell B_{\ell+1}}{\ell-1 \ell \quad \ell+1 \ell+2} \quad (5a)$$

$$(H_\ell^{\text{1s}} - E)\psi_\ell^{\text{1s}} = 0, \quad \text{Diagram} = E \frac{C_\ell}{\ell} \quad (5b)$$

Updating site by site, one sweeps back and forth through the MPS until the GS energy converges.

The local variational space is larger for 2s than 1s DMRG by a factor  $d$ ,  $\mathcal{O}(D^2d^2)$  vs.  $\mathcal{O}(D^2d)$ . This enables 2s DMRG to increase (“expand”) the bond dimension during updates by including new states (and symmetry sectors!) from the 2s space. 1s DMRG cannot do this, and hence often fails to yield accurate GS energies. The better performance of 2s vs. 1s has its price: much higher numerical costs,  $\mathcal{O}(D^3d^3 + D^3d^2w)$  vs.  $\mathcal{O}(D^3dw)$  [5].

*Discarded spaces.*— To track those parts of 2s spaces not contained in 1s spaces, we introduce orthogonal complements of  $A_\ell$  and  $B_\ell$ , denoted  $\overline{A}_\ell(\nabla)$  and  $\overline{B}_\ell(\nabla)$ . These isometries have image spaces, called *discarded* (D) spaces [25], of dimension  $\overline{D} = D(d-1)$ , orthogonal to the kept images of  $A_\ell$  and  $B_\ell$ . Thus  $A_\ell^{\perp}(\nabla) = A_\ell \oplus \overline{A}_\ell$  and  $B_\ell^{\perp}(\nabla) = B_\ell \oplus \overline{B}_\ell$  are unitaries on their parent spaces, with

$$\frac{A_\ell}{D \overline{D}} \oplus \frac{\overline{A}_\ell}{D \overline{D}} = \frac{A_\ell^{\perp}}{D \overline{D}}, \quad \frac{B_\ell^{\perp}}{D \overline{D}} = \frac{B_\ell}{D \overline{D}} \oplus \frac{\overline{B}_\ell}{D \overline{D}}. \quad (6)$$

The unitarity conditions for  $A_\ell^{\perp}$  and  $B_\ell^{\perp}$  imply orthonormality and completeness relations complementing Eq. (2),

$$\sum_{\ell} \left( = \mathbb{1}_\ell^D, \quad \sum_{\ell} = 0, \quad \sum_{\ell} = \right) = \mathbb{1}_{\ell-1}^D, \quad \sum_{\ell} = 0 \quad (7a)$$

$$\sum_{\ell} + \sum_{\ell} = \sum_{\ell} = \mathbb{1}_\ell^P, \quad \sum_{\ell} + \sum_{\ell} = \sum_{\ell} = \mathbb{1}_{\ell-1}^P. \quad (7b)$$

If the unitary maps  $A_\ell^{1\dagger}$  and  $B_{\ell+1}^{1\dagger}$  of Eq. (6) are applied to some of the open indices of  $H_\ell^{1s}\psi_\ell^{1s}$ ,  $H_{\ell+1}^{1s}\psi_{\ell+1}^{1s}$  and  $H_\ell^{2s}\psi_\ell^{2s}$  as indicated below, they map the diagrams of Eqs. (5) to

$$\begin{aligned} H_\ell^{1s}\psi_\ell^{1s} &\rightarrow \text{Diagram 1} = \text{Diagram 2} = \text{Diagram 3} \oplus \text{Diagram 4}, \\ H_{\ell+1}^{1s}\psi_{\ell+1}^{1s} &\rightarrow \text{Diagram 5} = \text{Diagram 6} = \text{Diagram 7} \oplus \text{Diagram 8}, \\ H_\ell^{2s}\psi_\ell^{2s} &\rightarrow \text{Diagram 9} \oplus \text{Diagram 10} \oplus \text{Diagram 11} \oplus \text{Diagram 12} \end{aligned}$$

The first three terms from the third line also appear in the first two lines, but the fourth, involving  $\Delta\Delta$ , does not. Let DD denote the image of the orthogonal complements  $\overline{A}_\ell \otimes \overline{B}_{\ell+1}(\nabla \otimes \nabla)$ , then DD is orthogonal to the variational space explored by 1s DMRG on sites  $(\ell, \ell+1)$ . DD is much larger than the latter, of dimension  $\overline{D}^2 = D^2(d-1)^2$  vs.  $2D^2d$ , and (importantly!) may contain new symmetry sectors. Thus DD is the 2s ingredient lacking in 1s schemes.

This can also be seen considering the energy variance  $\Delta_E = \|(H - E)\Psi\|^2$ . By expanding it into contributions involving orthogonal projections on one, two, or more sites [26],  $\Delta_E = \Delta_E^{1\perp} + \Delta_E^{2\perp} + \dots$ , one obtains [25]

$$\Delta_E^{1\perp} = \sum_{\ell=1}^{\mathcal{L}} \left\| \text{Diagram 1} \right\|^2, \quad \Delta_E^{2\perp} = \sum_{\ell=1}^{\mathcal{L}-1} \left\| \text{Diagram 2} \right\|^2. \quad (8)$$

1s DMRG minimizes only  $\Delta_E^{1\perp}$ , 2s minimizes  $\Delta_E^{1\perp}$  and  $\Delta_E^{2\perp}$ . We thus seek to expand the  $\nabla$  image of  $\nabla$  or  $\nabla$  at the

expense of the D image of  $\nabla$  or  $\nabla$ . This transfers weight from  $\Delta_E^{2\perp}$  to  $\Delta_E^{1\perp}$ , making it accessible to 1s minimization.

*Controlled bond expansion.*— The CBE algorithm rests on two new insights, substantiated by the quality of its results. The first insight is that the subspace of DD relevant for lowering the GS energy is relatively small: it is the subspace on which  $H_\ell^{2s}\psi_\ell^{2s}$  and hence  $\Delta_E^{2\perp}$  have significant weight. When expanding a bond, it thus suffices to add only this small subspace (hence the moniker *controlled bond expansion*), or only part of it, to be called relevant DD (RDD). Since DD is the image of  $\overline{A}_\ell \otimes \overline{B}_{\ell+1}(\nabla \otimes \nabla)$ , RDD can be viewed as the image of  $\widetilde{A}_\ell^{\text{tr}} \otimes \widetilde{B}_{\ell+1}(\nabla \otimes \nabla)$  or  $\overline{A}_\ell \otimes \widetilde{B}_{\ell+1}^{\text{tr}}(\nabla \otimes \nabla)$ , where the isometries  $\widetilde{A}_\ell^{\text{tr}}$  or  $\widetilde{B}_{\ell+1}^{\text{tr}}$  are *truncated* versions of  $\overline{A}_\ell$  or  $\overline{B}_{\ell+1}$  and have image dimensions  $\widetilde{D}$ , say. It turns out that one may choose  $\widetilde{D} < D$ , independent of  $d$ , thus RDD, of dimension  $\widetilde{D}D$ , is indeed much smaller than DD. The second insight is that  $\widetilde{A}_\ell^{\text{tr}}$  or  $\widetilde{B}_{\ell+1}^{\text{tr}}$  can be constructed at 1s costs using a novel scheme explained in Figs. 1 and 2. We call it *shrewd selection* since it is cheap, efficient and practical, though not strictly optimal (that would require 2s costs).

Based on these insights, a CBE update of bond  $\ell$  proceeds in four substeps. We describe them for a right-to-left sweep for building  $\widetilde{A}_\ell^{\text{tr}}$  and updating  $C_{\ell+1}$  (left-to-right sweeps, building  $\widetilde{B}_{\ell+1}^{\text{tr}}$  and updating  $C_\ell$ , are analogous).

(i) Compute  $\widetilde{A}_\ell^{\text{tr}}(\nabla)$  using shrewd selection.

(ii) Expand bond  $\ell$  from dimension  $D$  to  $D + \widetilde{D}$  by replacing  $A_\ell$  by an expanded isometry  $A_\ell^{\text{ex}}(\nabla) = A_\ell \oplus \widetilde{A}_\ell^{\text{tr}}$ , and  $C_{\ell+1}$  by an expanded tensor initialized as  $C_{\ell+1}^{\text{ex},i}(\nabla)$ , defined such that  $A_\ell^{\text{ex}}C_{\ell+1}^{\text{ex},i} = A_\ell C_{\ell+1}$ :

$$\frac{A_\ell}{D \overline{D}} \oplus \frac{\widetilde{A}_\ell^{\text{tr}}}{D \overline{D}} = \frac{A_\ell^{\text{ex}}}{D \overline{D}} \oplus \frac{C_{\ell+1}^{\text{ex},i}}{D \overline{D}} = \text{Diagram 13}. \quad (9)$$

Also construct an expanded one-site Hamiltonian, defined in a variational space of dimension  $D(D + \widetilde{D})d$ :

$$H_{\ell+1}^{1s,\text{ex}} = \text{Diagram 14} = \frac{D + \widetilde{D}}{D} \text{Diagram 15} \frac{d}{D} \text{Diagram 16}. \quad (10)$$

(iii) Update  $C_{\ell+1}^{\text{ex}}$  variationally by using an iterative eigensolver, as usual in DMRG, to find the GS solution of  $(H_{\ell+1}^{1s,\text{ex}} - E)C_{\ell+1}^{\text{ex}} = 0$ , starting from  $C_{\ell+1}^{\text{ex},i}$ . (We employ a Lanczos eigensolver.) This has costs of  $\mathcal{O}(D^3dw)$ . Thus,  $C_{\ell+1}^{\text{ex}}$  can be updated at 1s costs, while including only the most relevant 2s information via the contribution of  $\widetilde{A}_\ell^{\text{tr}}$ .

(iv) Shift the isometry center from site  $\ell+1$  to site  $\ell$  using a singular value decomposition (SVD) and truncate (trim) bond  $\ell$  from dimension  $D + \widetilde{D}$  back to  $D$ , removing low-weight states. The discarded weight, say  $\xi$ , of this bond trimming serves as error measure. It can be used for extrapolations, e.g. of GS energy versus  $\xi$ , just as for 2s DMRG. This yields GS energies comparable in accuracy to 2s DMRG or 2s variance extrapolations [26] (see below), though computing  $\xi$  requires only 1s costs.

$$\mathcal{C}_2 = \left\| \begin{array}{c} \text{Diagram 1} \\ \parallel \\ \text{Diagram 2} \end{array} - \begin{array}{c} \text{Diagram 3} \\ \parallel \\ \text{Diagram 4} \end{array} \right\|, \quad \mathcal{C}_3 = \left\| \begin{array}{c} \text{Diagram 5} \\ \parallel \\ \text{Diagram 6} \end{array} - \begin{array}{c} \text{Diagram 7} \\ \parallel \\ \text{Diagram 8} \end{array} \right\|.$$

FIG. 1. During a right-to-left CBE sweep, bond  $\ell$  is expanded from  $A_\ell(\nabla)$  to  $A_\ell \oplus \tilde{A}_\ell^{\text{tr}}(\nabla \oplus \nabla)$ , where  $\tilde{A}_\ell^{\text{tr}}(\nabla)$ , with image dimension  $\tilde{D}$ , is a truncation of  $\overline{A}_\ell(\nabla)$ , with image dimension  $\overline{D} = D(d-1)$ . This expansion will reduce  $\Delta_E^{2s}$  significantly if  $\tilde{A}_\ell^{\text{tr}} \oplus \overline{B}_{\ell+1}(\nabla \otimes \nabla)$  targets rDD, a  $\tilde{D}\overline{D}$ -dimensional subspace of the  $\overline{D}^2$ -dimensional space DD on which  $H_\ell^{2s}\psi_\ell^{2s}$  has significant weight. Ideally,  $\tilde{A}_\ell^{\text{tr}}$  should minimize the cost function  $\mathcal{C}_1$ , the difference between applying the projectors  $\overline{A}_\ell \overline{A}_\ell^\dagger$  or  $\tilde{A}_\ell^{\text{tr}} \tilde{A}_\ell^{\text{tr}\dagger}$  to  $H_\ell^{2s}\psi_\ell^{2s} \overline{B}_{\ell+1}^\dagger \overline{B}_{\ell+1}$ . However, exact minimization of  $\mathcal{C}_1$  would involve 2s costs (feasible if  $d, w$  and  $D$  are comparatively small, but in general undesirable). To maintain 1s costs,  $\mathcal{O}(D^3dw)$ , we instead use *shrewd selection*, involving two separate truncations (explained in Fig. 2, depicted schematically in Fig. 3). The first truncation (*preselection*) truncates the central MPS bond from  $D \rightarrow D'$  (specified below) in the presence of its environment by minimizing  $\mathcal{C}_2$ ; this replaces the full complement by a preselected complement,  $\overline{A}_\ell \nabla \rightarrow \tilde{A}_\ell^{\text{pr}} \nabla$ , with reduced image dimension,  $\overline{D} \rightarrow \tilde{D} = D'w$  [27]. The second truncation (*final selection*) minimizes  $\mathcal{C}_3$  with central MPO bond closed as appropriate for  $H_\ell^{2s}\psi_\ell^{2s}$ : it further truncates  $\tilde{A}_\ell^{\text{pr}}$  to yield the final truncated complement,  $\tilde{A}_\ell^{\text{tr}}, \nabla \rightarrow \nabla, \tilde{D} \rightarrow \tilde{D} < D$ . To ensure 1s costs for final selection we need  $\tilde{D} = D$ , and thus choose  $D' = D/w$  for preselection. Though shrewd selection involves severe bond reductions, it yields rDDs suitable for efficiently lowering the GS energy (in step (iii)). Section S-2 in [28] illustrates this by analysing singular value spectra.

The energy minimization based on  $H_{\ell+1}^{1s,\text{ex}}$  is variational, hence each CBE update strictly lowers the GS energy. Moreover, although CBE explores a much smaller variational space than 2s DMRG, it still converges at the same rate (as shown below), since it focuses on the subspace that really matters for energy reduction.

We remark that bond expansion using a truncated DD has been proposed before [24, 29]. But our choice of  $A_\ell^{\text{ex}}(\nabla)$  is more optimal than for the subspace expansion of Ref. [24], which requires a heuristic mixing factor and yields updates that sometimes raise the energy; and our method of finding  $A_\ell^{\text{ex}}(\nabla)$  at 1s costs is cheaper than that used in [29] (for the variational uniform MPS algorithm [30]), which uses an SVD requiring 2s costs.

*Sweeping.*— Our computations exploit non-Abelian symmetries [31, 32], where bond dimensions, denoted  $D^*$ , count symmetry multiplets ( $D$  counts states). Usually,  $D^*$  is increased with each update during sweeping, from an initial  $D_i^*$  to a final  $D_f^* = \alpha D_i^*$ , with  $\alpha > 1$ . To achieve this with using CBE, we (i,ii) use  $D'^* \simeq D_f^*/w^*$ ,  $\tilde{D}^* = D_f^*$  (cf. Fig. 2) and expand from  $D_i^*$

$$D_i^* + \tilde{D}^* = D_f^*(1 + \delta), \quad (11)$$

(iii) call the iterative eigensolver, and (iv) truncate back

$$\begin{aligned} A_\ell \downarrow \Lambda_\ell B_{\ell+1} &= \begin{array}{c} \text{Diagram 1} \\ \parallel \\ \text{Diagram 2} \end{array} \xrightarrow{\text{SVD}} \begin{array}{c} \text{Diagram 3} \\ \parallel \\ \text{Diagram 4} \end{array} \xrightarrow{\text{truncation}} \begin{array}{c} \text{Diagram 5} \\ \parallel \\ \text{Diagram 6} \end{array} \\ &\xrightarrow{\text{SVD}} \begin{array}{c} \text{Diagram 7} \\ \parallel \\ \text{Diagram 8} \end{array} \xrightarrow{\text{truncation}} \begin{array}{c} \text{Diagram 9} \\ \parallel \\ \text{Diagram 10} \end{array} \\ &\xrightarrow{\text{SVD}} \begin{array}{c} \text{Diagram 11} \\ \parallel \\ \text{Diagram 12} \end{array} \xrightarrow{\text{truncation}} \begin{array}{c} \text{Diagram 13} \\ \parallel \\ \text{Diagram 14} \end{array} \end{aligned}$$

FIG. 2. Shrewd selection: Computation of (a-c) the preselected complement  $\tilde{A}_\ell^{\text{pr}}(\nabla)$  to minimize  $\mathcal{C}_2$ , and (d) the final truncated complement  $\tilde{A}_\ell^{\text{tr}}(\nabla)$  to minimize  $\mathcal{C}_3$ , using four SVDs, all with at most 1s costs. For each, an arrow indicates a bond being opened before doing the SVD, shading and symbols in matching colors indicate the SVD input and output, and the latter is written as  $USV^\dagger$  or  $usv^\dagger$  when involving no or some truncation, respectively. Importantly, we express  $\overline{A}_\ell \overline{A}_\ell^\dagger$  and  $\overline{B}_{\ell+1}^\dagger \overline{B}_{\ell+1}$  (grey) as  $\mathbb{1}_\ell^P - A_\ell A_\ell^\dagger$  and  $\mathbb{1}_\ell^P - B_{\ell+1}^\dagger B_{\ell+1}$  (Eq. (7b)), avoiding the computation of  $\overline{A}_\ell$  and  $\overline{B}_{\ell+1}$ . (a) The first SVD canonicalizes the right side of the diagram, assigning its weights to the central MPS bond. (b) The second SVD and truncation reduces the dimension of this bond,  $D \rightarrow D' = D/w$ . (c) The third SVD regroups indices to combine the truncated MPS bond and the MPO bond into a composite bond of dimension  $\tilde{D} = D'w = D$ , yielding the preselected complement  $\tilde{A}_\ell^{\text{pr}} = \tilde{U}(\nabla)$ . Nominally, step (c) would require no truncation if exact arithmetic were used, but in practice (numerically) zero singular values, of order  $\mathcal{O}(10^{-16})$ , may arise; these must be discarded to ensure  $A_\ell^\dagger \tilde{A}_\ell^{\text{pr}} = 0$ . (d) The fourth SVD and truncation yields the final truncated complement  $\tilde{A}_\ell^{\text{tr}} = \tilde{A}_\ell^{\text{pr}} \tilde{u}(\nabla)$ , with bond reduction  $\tilde{D} \rightarrow \tilde{D} < D$ .

to  $D_f^*$  when shifting the isometry center. We use  $\alpha = \sqrt{2}$  and  $\delta = 0.1$  (for CBE), unless stated otherwise. For the CBE and 2s DMRG comparisons shown below, we use the same initial state: a  $D_i^* = 1$  valence bond state with one fermion per site, uniform density and total spin 0.

*Results.*— We now benchmark CBE–DMRG for free fermions in one dimension (1D), then illustrate its performance for computationally challenging models: the 1D Hubbard–Holstein model and the 2D Hubbard and Kondo–Heisenberg–Holstein models on cylinders. We choose not to discuss their rich physics, aiming here only to demonstrate the feasibility of studying them with CBE–DMRG.

All CPU time measurements were done on a single core of an Intel Core i7-9750H processor.

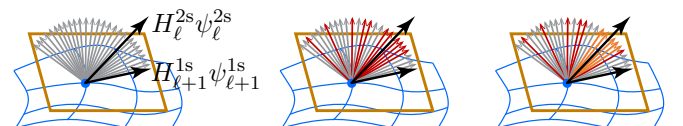


FIG. 3. The projection  $H_\ell^{2s}\psi_\ell^{2s} \xrightarrow{A_\ell^\dagger} H_{\ell+1}^{1s}\psi_{\ell+1}^{1s}$  to the tangent space (yellow) of the MPS manifold (blue) discards information from DD (depicted by grey arrows for DD basis vectors). Relevant information is recovered at 1s cost by constructing rDD through preselection (red), then final selection (orange).

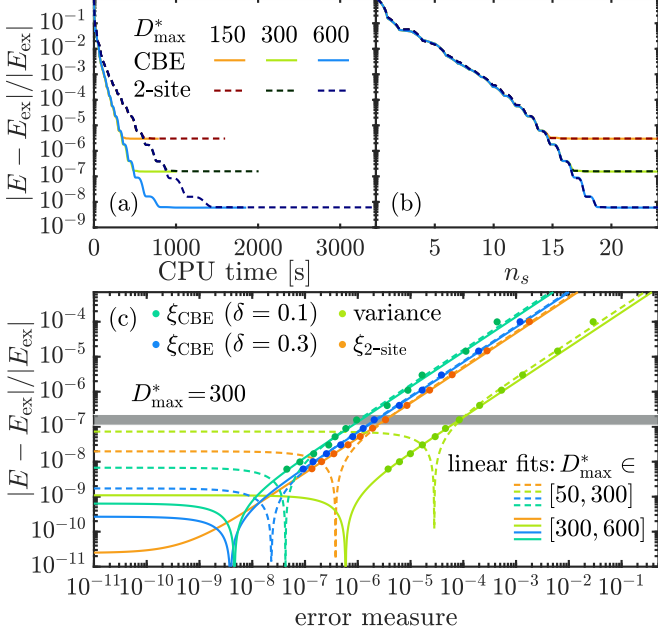


FIG. 4. Relative error in GS energy vs. (a) CPU time and (b) number of half-sweeps  $n_s$ , for CBE and 2s DMRG.  $E_{\text{ex}}$  is the exact GS energy. (c) Quality of linear extrapolation of the GS energy using various error measures. Dashed (solid) lines show linear fits to data points lying on or above (on or below) the grey bar, computed using  $D_{\text{max}}^* \leq 300$  ( $\geq 300$ ), representing intermediate (high) accuracy calculations; when these lines touch zero, the extrapolated error changes sign.

*Free fermions.*— To benchmark our CBE scheme, we consider a chain of spinful free fermions, exactly solvable but non-trivial for DMRG, with Hamiltonian  $H_{\text{ff}} = -\sum_{i=1}^{\mathcal{L}-1} \sum_{\sigma} (c_{i\sigma}^\dagger c_{i+1\sigma} + \text{h.c.})$  and  $\mathcal{L} = 100$  sites. We exploit  $U(1)_{\text{ch}} \otimes \text{SU}(2)_{\text{sp}}$  charge and spin symmetry, with local dimension  $d^*[d] = 3[4]$ . The MPO dimension is  $w^*[w] = 4[6]$ . We seek the GS in the sector with total spin  $S=0$ , at half-filling, with particle number  $N=\mathcal{L}$ .

Figure 4(a) plots the relative error in energy vs. CPU time for different  $D_{\text{max}}^*$  for both CBE and 2s schemes; Fig. 4(b) plots it vs. the number of half-sweeps  $n_s$ . While convergence with  $n_s$  is comparable for CBE and 2s, CBE requires less CPU time than 2s by a factor of  $\simeq 2$ . (This speedup factor is less than  $d^* = 3$ , since  $d^*$  is quite small and steps not involving the iterative eigensolver have the same numerical cost for both CBE and 2s schemes.)

Figure 4(c) shows linear-fit extrapolations of the energy in terms of the discarded weight  $\xi$  and the 2s variance (the latter computed following Ref. [26]). The quality of the extrapolations is comparable for all considered methods: they all reduce the error in energy by roughly one order compared to the most accurate data point considered, as expected [23, 26]. The error is smaller for  $\delta = 0.3$  than for  $\delta = 0.1$ , and its dependence on discarded weight slightly less noisy (though this hardly affects the extrapolation).

*Hubbard-Holstein model (chain).*— As a more challenging application, we consider interacting spinful electrons on a 1D chain coupled to phonons [33–37], described

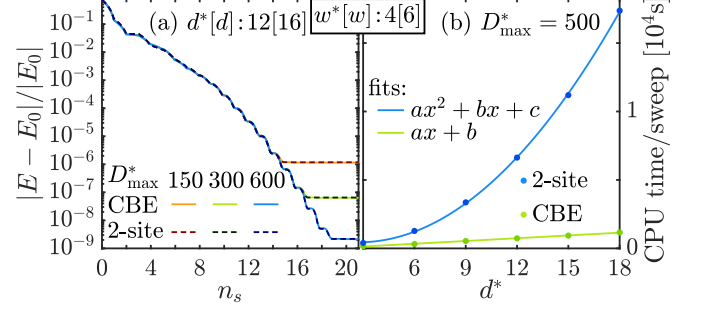


FIG. 5. Hubbard-Holstein model: (a) Convergence of the GS energy versus number of half-sweeps  $n_s$  at fixed  $d^* = 3(N_{\text{ph}}^{\text{max}} + 1)$ .  $E_0$  was obtained by linear  $\xi$ -extrapolation of data from  $D_{\text{max}}^* \in [1000, 1200]$ . (b) CPU time per sweep for different  $d^*$  at fixed  $D_{\text{max}}^*$ , showing  $d^*$  vs.  $d^{*2}$  scaling for the CBE vs. 2s algorithms.

by the Hamiltonian  $H_{\text{HH}} = -\sum_{i\sigma} (c_{i\sigma}^\dagger c_{i+1\sigma} + \text{h.c.}) + U \sum_i n_{i\uparrow} n_{i\downarrow} + \omega_{\text{ph}} \sum_i b_i^\dagger b_i + g \sum_i (n_{i\uparrow} + n_{i\downarrow} - 1) (b_i^\dagger + b_i)$ . We chose  $U = 0.8$ ,  $g = \sqrt{0.2}$ ,  $\omega_{\text{ph}} = 0.5$ ,  $\mathcal{L} = N = 50$  half-filled sites, total spin  $S=0$ , and restricted the maximum local number of excited phonons to  $N_{\text{ph}}^{\text{max}}$ . Then,  $d^*[d] = 3(N_{\text{ph}}^{\text{max}} + 1) [4(N_{\text{ph}}^{\text{max}} + 1)]$  and  $w^*[w] = 4[6]$ .

Figure 5(a) shows the relative error in energy vs. number of half-sweeps  $n_s$  for different  $D_{\text{max}}^*$  at fixed  $d^* = 12$ , comparing CBE and 2s schemes. The convergence with  $n_s$  is again similar for CBE and 2s. Figure 5(b) compares the CPU time per sweep for CBE and 2s for different  $d^*$  at fixed  $D_{\text{max}}^*$ . Linear and quadratic fits confirm the expected  $d^*$  or  $d^{*2}$  scaling, respectively, showing unambiguously that CBE indeed has 1s scaling.

*Fermionic models on cylinders.*— To check the ability of CBE-DMRG to deal with very challenging models, we have also tested it on fermionic models on  $10 \times 4$  cylinders, exploiting  $U(1)_{\text{ch}} \otimes \text{SU}(2)_{\text{sp}}$  charge and spin symmetries. As a benchmark, we have considered the Hubbard model up to  $D^* = 12000$  where we find good agreement with data from Ref. 26. We then considered a more challenging Kondo-Heisenberg-Holstein model, which features physical and MPO bond-dimensions from  $d^*[d] = 4[8]$  and  $w^*[w] = 10[16]$  (up to  $D^* = 15000$ ) up to  $d^*[d] = 16[32]$  and  $w^*[w] = 14[30]$  (up to  $D^* = 7000$ ), respectively. More information and data demonstrating stable convergence of CBE-DMRG is shown in the supplemental material [28].

*Summary and outlook.*— CBE expands bonds by adding subspaces on which  $\Delta_E^{2s}$ , the 2s contribution to the energy variance, has significant weight, thus making these subspaces accessible to 1s energy minimization. The above results show that CBE yields 2s accuracy and convergence per sweep, at 1s costs. In contrast to previous 1s methods, CBE avoids mixing parameters and is fully variational (up to bond trimming when shifting the isometry center). It has 1s costs, since the variational space is only slightly expanded relative to 1s DMRG. 2s convergence is achieved since the bond expansion is *controlled*, targeting only highly relevant parts of the 2s variational

space contributing strongly to the energy variance  $\Delta_E^{2s}$ . Using *shrewd selection*, these can be identified at 1s costs.

Due to its significant costs savings, CBE opens the door to studying challenging models of current interest at higher accuracy (larger  $D$ ) than previously possible, or tackling more complex models, with  $d$  or  $w$  so large that they were hitherto out of reach. Examples are multi-band models with several different type of couplings, in particular in two-dimensional settings, models involving bosonic excitations, and quantum-chemical applications.

More generally, CBE can be used in any context requiring variational optimization of an MPS. Apart from energy minimization, an example is approximating a given  $\Psi$  by a  $\Psi'$  with smaller bond dimension through minimization of  $\|\Psi' - \Psi\|$ . CBE can also be used to build Krylov spaces with 2s accuracy at 1s costs, thus impacting all of the large variety of MPS methods relying on Krylov methods. For example, in a follow-up paper [38] we focus on MPS time evolution using the time-dependent variational principle (TDVP), and use CBE to achieve dramatic improvements in performance. Finally, analogous statements hold for contexts involving the variational optimization or the time evolution of MPOs. We thus expect that CBE will be widely used and become an indispensable tool in the MPS/MPO toolbox.

We thank Andreas Weichselbaum for stimulating discussions, and Seung-Sup Lee, Juan Espinoza, Matan Lotem, Jeongmin Shim and Andreas Weichselbaum for helpful comments on our manuscript. Our numerical simulations employed the QSpace tensor library [31, 32]. This research was funded in part by the Deutsche Forschungsgemeinschaft under Germany's Excellence Strategy EXC-2111 (Project No. 390814868), and is part of the Munich Quantum Valley, supported by the Bavarian state government with funds from the Hightech Agenda Bayern Plus.

malization group study of the striped phase in the 2d  $t - J$  model, *Phys. Rev. Lett.* **80**, 1272 (1998).

- [9] S. R. White and D. J. Scalapino, Checkerboard patterns in the  $t-j$  model, *Phys. Rev. B* **70**, 220506 (2004).
- [10] S. R. White and D. J. Scalapino, Pairing on striped  $t-t'-J$  lattices, *Phys. Rev. B* **79**, 220504 (2009).
- [11] S. Jiang, D. J. Scalapino, and S. R. White, Ground-state phase diagram of the  $t-t'-J$  model, *Proceedings of the National Academy of Sciences* **118**, e2109978118 (2021).
- [12] J. P. F. LeBlanc, A. E. Antipov, F. Becca, I. W. Bulik, G. K.-L. Chan, C.-M. Chung, Y. Deng, M. Ferrero, T. M. Henderson, C. A. Jiménez-Hoyos, E. Kozik, X.-W. Liu, A. J. Millis, N. V. Prokof'ev, M. Qin, G. E. Scuseria, H. Shi, B. V. Svistunov, L. F. Tocchio, I. S. Tupitsyn, S. R. White, S. Zhang, B.-X. Zheng, Z. Zhu, and E. Gull (Simons Collaboration on the Many-Electron Problem), Solutions of the two-dimensional Hubbard model: Benchmarks and results from a wide range of numerical algorithms, *Phys. Rev. X* **5**, 041041 (2015).
- [13] G. Ehlers, S. R. White, and R. M. Noack, Hybrid-space density matrix renormalization group study of the doped two-dimensional Hubbard model, *Phys. Rev. B* **95**, 125125 (2017).
- [14] B.-X. Zheng, C.-M. Chung, P. Corboz, G. Ehlers, M.-P. Qin, R. M. Noack, H. Shi, S. R. White, S. Zhang, and G. K.-L. Chan, Stripe order in the underdoped region of the two-dimensional Hubbard model, *Science* **358**, 1155 (2017), arXiv:1701.00054 [cond-mat.str-el].
- [15] E. W. Huang, C. B. Mendl, H.-C. Jiang, B. Moritz, and T. P. Devereaux, Stripe order from the perspective of the Hubbard model, *npj Quantum Materials* **3**, 22 (2018).
- [16] M. Qin, C.-M. Chung, H. Shi, E. Vitali, C. Hubig, U. Schollwöck, S. R. White, and S. Zhang (Simons Collaboration on the Many-Electron Problem), Absence of superconductivity in the pure two-dimensional Hubbard model, *Phys. Rev. X* **10**, 031016 (2020).
- [17] Y.-F. Jiang, J. Zaanen, T. P. Devereaux, and H.-C. Jiang, Ground state phase diagram of the doped Hubbard model on the four-leg cylinder, *Phys. Rev. Research* **2**, 033073 (2020).
- [18] H.-C. Jiang and S. A. Kivelson, Stripe order enhanced superconductivity in the Hubbard model, *PNAS* **119**, e2109406119 (2022).
- [19] S. Yan, D. A. Huse, and S. R. White, Spin-liquid ground state of the  $S = 1/2$  kagome Heisenberg antiferromagnet, *Science* **332**, 1173 (2011).
- [20] S. Depenbrock, I. P. McCulloch, and U. Schollwöck, Nature of the spin-liquid ground state of the  $S = 1/2$  Heisenberg model on the kagome lattice, *Phys. Rev. Lett.* **109**, 067201 (2012).
- [21] F. Kolley, S. Depenbrock, I. P. McCulloch, U. Schollwöck, and V. Alba, Phase diagram of the  $J_1-J_2$  Heisenberg model on the kagome lattice, *Phys. Rev. B* **91**, 104418 (2015).
- [22] Y.-C. He, M. P. Zaletel, M. Oshikawa, and F. Pollmann, Signatures of dirac cones in a DMRG study of the kagome Heisenberg model, *Phys. Rev. X* **7**, 031020 (2017).
- [23] S. R. White, Density matrix renormalization group algorithms with a single center site, *Phys. Rev. B* **72**, 180403 (2005).
- [24] C. Hubig, I. P. McCulloch, U. Schollwöck, and F. A. Wolf, Strictly single-site DMRG algorithm with subspace expansion, *Phys. Rev. B* **91**, 155115 (2015).
- [25] A. Gleis, J.-W. Li, and J. von Delft, Projector formalism

---

- [1] S. R. White, Density matrix formulation for quantum renormalization groups, *Phys. Rev. Lett.* **69**, 2863 (1992).
- [2] S. R. White, Density-matrix algorithms for quantum renormalization groups, *Phys. Rev. B* **48**, 10345 (1993).
- [3] F. Verstraete, D. Porras, and J. I. Cirac, Density matrix renormalization group and periodic boundary conditions: A quantum information perspective, *Phys. Rev. Lett.* **93**, 227205 (2004).
- [4] U. Schollwöck, The density-matrix renormalization group, *Rev. Mod. Phys.* **77**, 259 (2005).
- [5] U. Schollwöck, The density-matrix renormalization group in the age of matrix product states, *Annals of Physics* **326**, 96 (2011).
- [6] S. R. White, Spin gaps in a frustrated Heisenberg model for cav409, *Phys. Rev. Lett.* **77**, 3633 (1996).
- [7] E. Stoudenmire and S. R. White, Studying two-dimensional systems with the density matrix renormalization group, *Ann. Rev. Cond. Mat. Phys.* **3**, 111 (2012).
- [8] S. R. White and D. J. Scalapino, Density matrix renor-

for kept and discarded spaces of matrix product states, [arXiv:2207.13161 \[quant-ph\]](https://arxiv.org/abs/2207.13161) (2022).

[26] C. Hubig, J. Haegeman, and U. Schollwöck, Error estimates for extrapolations with matrix-product states, *Phys. Rev. B* **97**, 045125 (2018).

[27] We could achieve the desired reduction  $\bar{D} \rightarrow \tilde{D}$  already during preselection by choosing  $D' = \tilde{D}/w$  there, so that  $\hat{D} = \bar{D}$ ; however, that would neglect the information that in  $H^{2s}\psi^{2s}$  the central MPO bond is closed. Final selection serves to include that information.

[28] See Supplemental Material at [url] for an analysis of singular value spectra obtained from shrewd selection; numerical results for fermionic models defined on cylinders; and a pseudocode for shrewd selection. The Supplemental Material includes Refs. [13, 26, 39–43].

[29] V. Zauner-Stauber, L. Vanderstraeten, M. T. Fishman, F. Verstraete, and J. Haegeman, Variational optimization algorithms for uniform matrix product states, *Phys. Rev. B* **97**, 045145 (2018).

[30] L. Vanderstraeten, J. Haegeman, and F. Verstraete, Tangent-space methods for uniform matrix product states, *SciPost Phys. Lect. Notes* **7** (2019).

[31] A. Weichselbaum, Non-abelian symmetries in tensor networks: A quantum symmetry space approach, *Ann. of Phys.* **327**, 2972 (2012).

[32] A. Weichselbaum, X-symbols for non-abelian symmetries in tensor networks, *Phys. Rev. Research* **2**, 023385 (2020).

[33] E. Jeckelmann and S. R. White, Density-matrix renormalization-group study of the polaron problem in the Holstein model, *Phys. Rev. B* **57**, 6376 (1998).

[34] M. Tezuka, R. Arita, and H. Aoki, Phase diagram for the one-dimensional Hubbard-Holstein model: A density-matrix renormalization group study, *Phys. Rev. B* **76**, 155114 (2007).

[35] H. Fehske, G. Hager, and E. Jeckelmann, Metallicity in the half-filled Holstein-Hubbard model, *E. J. Phys.* **84**, 57001 (2008).

[36] S. Ejima and H. Fehske, DMRG analysis of the sdw-cdw crossover region in the 1d half-filled Hubbard-Holstein model, *J. Phys.: Conference Series* **200**, 012031 (2010).

[37] T. E. Reinhard, U. Mordovina, C. Hubig, J. S. Kretschmer, U. Schollwöck, H. Appel, M. A. Sentef, and A. Rubio, Density-matrix embedding theory study of the one-dimensional Hubbard-Holstein model, *J. Chem. Theory and Comp.* **15**, 2221 (2019).

[38] J.-W. Li, A. Gleis, and J. von Delft, Time-dependent variational principle with controlled bond expansion for matrix product states, to be published (2022).

[39] J. Motruk, M. P. Zaletel, R. S. K. Mong, and F. Pollmann, Density matrix renormalization group on a cylinder in mixed real and momentum space, *Phys. Rev. B* **93**, 155139 (2016).

[40] P. Coleman, Heavy fermions: Electrons at the edge of magnetism, in *Handbook of Magnetism and Advanced Magnetic Materials*, Vol. 1, edited by H. Kronmüller and S. Parkin (Wiley, 2007) pp. 95–148.

[41] M. Ye, H.-H. Kung, P. F. S. Rosa, E. D. Bauer, K. Haule, and G. Blumberg, Anisotropy of Kondo-lattice coherence in momentum space for CeCoIn<sub>5</sub>, [arXiv:2202.09642 \[cond-mat.str-el\]](https://arxiv.org/abs/2202.09642) (2022).

[42] P. Coleman, C. Pépin, Q. Si, and R. Ramazashvili, How do Fermi liquids get heavy and die?, *J. Phys. Cond. Mat.* **13**, R723 (2001).

[43] J. M. Luttinger, Fermi surface and some simple equilibrium properties of a system of interacting fermions, *Phys. Rev.* **119**, 1153 (1960).

## Supplemental material:

### Controlled bond expansion for DMRG ground state search at single-site costs

Andreas Gleis,<sup>1</sup> Jheng-Wei Li,<sup>1</sup> and Jan von Delft<sup>1</sup>

<sup>1</sup>Arnold Sommerfeld Center for Theoretical Physics, Center for NanoScience, and Munich Center for Quantum Science and Technology, Ludwig-Maximilians-Universität München, 80333 Munich, Germany

(Dated: August 1, 2022)

This supplement offers additional material on three issues: in Sec. S-1, a detailed analysis of preselection and final selection; in Sec. S-2, numerical results illustrating the performance of CBE-DMRG for very challenging models (the Hubbard model and the Kondo-Heisenberg-Holstein model, both defined on a cylinder); and in Sec. S-3, a pseudocode for constructing the truncated complement using shrewd selection.

#### S-1. SHREWD SELECTION

Figures 1 and 2 in the main text discuss a novel scheme, called *shrewd selection*, needed for CBE. It involves two separate truncations, called *preselection* and *final selection*. In this section we discuss these in more detail, and illustrate their effects on the properties of various singular value spectra and singular vectors. We here write bond dimensions with  $*$ , indicating numbers of multiplets (not states), since these determine computational complexities and truncation thresholds and are the quantities shown in the figures. Relations such as  $\widehat{D} = D'w$ , exact for Abelian symmetries where all symmetry multiplets have dimension 1, become approximate,  $\widehat{D}^* \simeq D'^*w^*$ , when written for non-Abelian symmetries.

##### A. Options for preselection and final selection

The key idea of CBE is to expand the isometry  $A_\ell(\nabla)$ , whose image (the kept space) initially has dimension  $D_i^*$ , through a direct sum with a so-called truncated complement, an isometry with image dimension  $\widetilde{D}^*$  ( $< D_i^*$ ). The latter is obtained through a suitable truncation of the full complement,  $\widehat{A}_\ell(\nabla)$ , whose image (the discarded space) initially has dimension  $\overline{D}^* \simeq D_i^*(d^* - 1)$ . Figure 1 defines three cost functions,  $\mathcal{C}_1$ ,  $\mathcal{C}_2$  and  $\mathcal{C}_3$ , relevant for constructing the truncated complement. The optimal choice for the truncated complement, to be denoted  $\widehat{A}_\ell^{\text{tr}}(\nabla)$  here, is obtained by exact minimization of  $\mathcal{C}_1$ , but that requires 2s costs. Therefore, the main text proposes an alternative two-step strategy, requiring only 1s costs. First perform preselection: obtain a preselected complement  $\widehat{A}_\ell^{\text{pr}}(\nabla)$ , with image dimension  $\widehat{D}^* \simeq D'^*w^*$ , through minimization of  $\mathcal{C}_2$  (Fig. 2, steps (a-c)). Then perform final selection: obtain the desired truncated complement, denoted  $\widehat{A}_\ell^{\text{tr}}(\nabla)$ , through minimization of  $\mathcal{C}_3$  (Fig. 2, step (d)).

The minimization of the cost functions  $\mathcal{C}_1$  and  $\mathcal{C}_3$  defined in Fig. 1 involves performing SVDs and truncations of the following two tensors:

$$\overline{M}^{\text{full}} = \begin{array}{c} \text{Diagram} \\ \ell \\ \ell+1 \end{array} = \begin{bmatrix} \overline{U} & \overline{S} & \overline{V}^\dagger \\ \overline{D}^* & & \overline{D}^* \\ \overline{D}^* & & \overline{D}^* \end{bmatrix}_{d^*} \simeq \begin{bmatrix} \overline{u} & \overline{s} & \overline{v}^\dagger \\ \overline{D}^* & & \overline{D}^* \\ \overline{D}^* & & \overline{D}^* \end{bmatrix}_{d^*}, \quad (\text{S1a})$$

$$\widehat{M}^{\text{pr}} = \begin{array}{c} \text{Diagram} \\ \ell \\ \ell+1 \end{array} = \begin{bmatrix} \widetilde{U} & \widetilde{S} & \widetilde{V}^\dagger \\ \widehat{D}^* & & \widehat{D}^* \\ \widehat{D}^* & & \widehat{D}^* \end{bmatrix}_{d^*} \simeq \begin{bmatrix} \widetilde{u} & \widetilde{s} & \widetilde{v}^\dagger \\ \widehat{D}^* & & \widehat{D}^* \\ \widehat{D}^* & & \widehat{D}^* \end{bmatrix}_{d^*}. \quad (\text{S1b})$$

They differ only in one ingredient,  $\overline{A}_\ell(\nabla)$  vs.  $\widehat{A}_\ell^{\text{pr}}(\nabla)$ , but since these have vastly different open leg dimensions,  $\overline{D}^*$  vs.  $\widehat{D}^*$ , the SVD costs differ vastly too, 2s vs. 1s. The isometries  $\overline{u}(\nabla)$  or  $\widetilde{u}(\nabla)$  obtained from the above SVDs and truncations, both with image dimension  $\widetilde{D}^*$ , can then be used to construct  $\overline{A}_\ell^{\text{tr}}(\nabla)$  or  $\widetilde{A}_\ell^{\text{tr}}(\nabla)$  as follows:

$$\frac{\overline{A}_\ell^{\text{tr}}}{\overline{D}^* \nabla \widetilde{D}^*} = \frac{\overline{A}_\ell \overline{u}}{\nabla}, \quad (\text{S2a})$$

$$\frac{\widetilde{A}_\ell^{\text{tr}}}{\overline{D}^* \nabla \widetilde{D}^*} = \frac{\widehat{A}_\ell^{\text{pr}} \widetilde{u}}{\nabla}. \quad (\text{S2b})$$

Both  $\overline{A}_\ell^{\text{tr}}(\nabla)$  and  $\widetilde{A}_\ell^{\text{tr}}(\nabla)$  have image dimension  $\widetilde{D}^*$ ; the former serves as reference (equivalent to using no preselection,  $D'^* = D^*$ ), the latter is an approximation to the former. An even cruder approximation is obtained if one performs preselection without final selection: for that, truncate  $\widehat{U} \simeq \widehat{u}$  in step (c) of Fig. 2 using  $\widehat{D}^* = \widetilde{D}^*$  (not  $D'^*w^*$ ), and use the resulting isometry,  $\widehat{A}_\ell^{\text{tr}}(\nabla) = \widehat{u}$ , as approximation for  $\overline{A}_\ell^{\text{tr}}(\nabla)$ , omitting step (d) altogether:

$$\frac{\widehat{A}_\ell^{\text{tr}}}{\overline{D}^* \nabla \widetilde{D}^*} = -\frac{\widehat{u}}{\nabla}. \quad (\text{S2c})$$

To illustrate the effects of preselection, we will compare four settings: (I) the reference,  $\overline{A}^{\text{tr}}(\nabla)$ ; or three versions of preselection with  $D'^* = D_f^*/w^*$ ,  $0.1D_f^*/w^*$  or 1, to be called (II) *moderate*, (III) *severe* or (IV) *extreme* preselection, respectively, all followed by final selection, yielding three versions of  $\widetilde{A}^{\text{tr}}(\nabla)$ . Here,  $D_f^*$  is the final bond dimension after an update, obtained by expanding

the bond from dimension  $D_i^*$  to  $D_i^* + \tilde{D}^* = D_f^*(1+\delta)$ , then trimming it back to  $D_f^*$ . To illustrate the importance of final selection we also consider a fifth setting: (V) moderate preselection and  $\hat{U} \simeq \hat{u}$  truncation, without final selection, yielding  $\hat{A}_\ell^{\text{tr}}(\textcolor{violet}{\nabla})$ .

In the main text, we recommended performing CBE updates using moderate preselection followed by final selection. We showed (Fig. 4(a)) that this yields equally fast convergence per sweep for the GS energy as 2s update. Below, we elucidate why moderate preselection works so well. To this end, we analyze various singular value spectra (Sec. S-1 B) and left singular vectors (Sec. S-1 C), with  $D_f^* = D_{\max}^*$  fixed. We also show that severe and even extreme preselection likewise yield full convergence, albeit at slower rates, by comparing various convergence rates per sweep while increasing  $D_f^*$  (Sec. S-1 D).

## B. Singular values

We start by comparing the singular values of the tensors  $\bar{M}^{\text{full}}$  and  $\hat{M}^{\text{pr}}$ , i.e. the diagonal elements of the diagonal matrices  $\bar{S}(\textcolor{blue}{\downarrow})$  and  $\hat{S}(\textcolor{blue}{\downarrow})$  in Eqs. (S1), denoted  $\bar{S}_i$  ( $i = 1, \dots, \bar{D}^*$ ) and  $\hat{S}_i$  ( $i = 1, \dots, \tilde{D}^*$ ), respectively. They differ strongly in number, but if the largest  $\hat{S}_i$  values roughly mimic the largest  $\bar{S}_i$  values, serving as reference, then preselection is “efficient”, in that it yields essentially optimal results for the dominant singular values.

Figure S-1 compares  $\bar{S}_i$  (grey) and  $\hat{S}_i$  (orange: moderate or brown: severe preselection) for bond  $\ell = \mathcal{L}/2$  of both the least and most challenging models considered in this work: (a,b) the free fermion chain of Fig. 3, and (c,d) the KHH cylinder of Fig. S-5. Here, we consider the case that  $D_f^*$  has reached  $D_{\max}^*$  and is not grown further, and hence choose  $\tilde{D}^* = D_f^* \delta$  (with  $\delta = 0.1$ ), so that  $D_i^* = D_f^*$ .

For (II) moderate preselection ( $D'^* = D_f^*/w^*$ ) the  $\hat{S}_i$  (orange) and  $\bar{S}_i$  (grey) values coincide quite well in the range where they are largest, and eventually drift apart as they get smaller. Especially for the largest  $\tilde{D}^* = D_f^* \delta$  ( $\delta = 0.1$ ) singular values, i.e. the ones that survive final selection and are used for bond expansion, the agreement is rather good (Figs. S-1 (b,d)). This is a very important finding—it indicates that moderate preselection is efficient. By contrast, (III) severe preselection ( $D'^* = 0.1D_f^*/w^*$ ), shown only in Fig. S-1 (a,b), yields  $\hat{S}_i$  (brown) values that differ substantially from their  $\bar{S}_i$  (grey) counterparts, even in the range of largest values. Therefore, in this case preselection is too severe to be very efficient.

(We note in passing that when using severe preselection, the corresponding final selection involves almost no further truncation, since  $\hat{D}^*$  (given by  $\simeq D'^* w^* = 0.1 D^*$ ) is almost equal to  $\tilde{D}^*$  (given by  $D^* \delta$ ). For the present example, we have  $\hat{D}^* = 63$  and  $\tilde{D}^* = 60$ .)

In Figs. S-1 (a,b), the length of the grey vs. orange lines visually illustrates the main rationale for our CBE strat-

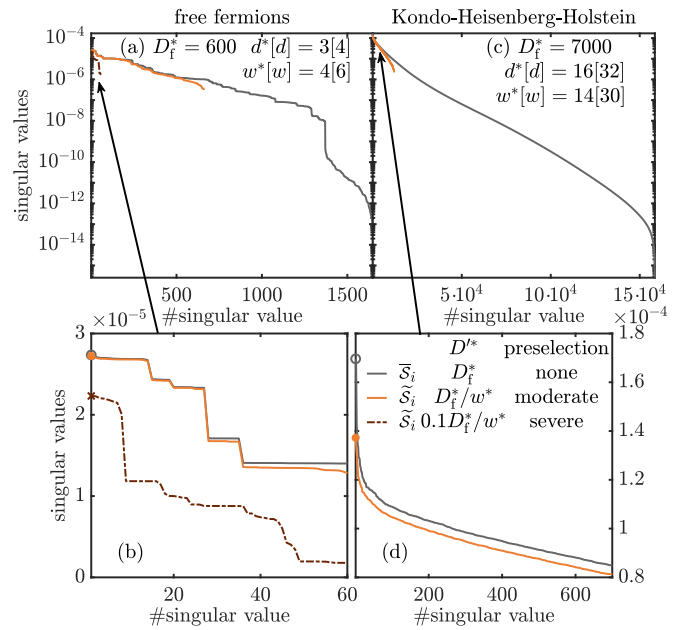


FIG. S-1. Comparison of singular values for three truncation settings (I-III) defined in Sec. S-1 A: the singular values  $\bar{S}_i$  of the tensor  $\bar{M}^{\text{full}}$ , obtained (I) without preselection (reference, grey); and the singular values  $\hat{S}_i$  of the tensor  $\hat{M}^{\text{pr}}$ , obtained using (II) moderate preselection ( $D'^* = D_f^*/w^*$ , orange) and (III) severe preselection ( $D'^* = 0.1D_f^*/w^*$ , brown), all followed by final selection with  $\tilde{D}^* = 0.1D_f^*$ . They are all computed for bond  $\ell = \mathcal{L}/2$  of (a,b) the free fermion chain of Fig. 3, and (c,d) the KHH cylinder of Fig. S-5(d). (b,d) Subsets of the data from (a,c), shown on linear scales, focusing on the range of the largest  $\tilde{D}^* = D_f^* \delta$  singular values  $\bar{S}_i$  and  $\hat{S}_i$  (with  $\delta = 0.1$ ). This range contains all singular vectors comprising the truncated complement  $\hat{A}_\ell^{\text{tr}}(\textcolor{violet}{\nabla})$  obtained after final selection and used for bond expansion. The singular values found with moderate (orange) or no (grey) preselection agree rather well, but those from severe preselection (brown) differ significantly from these.

egy: the number of  $\bar{S}_i$  values is generally very much larger than needed for successful bond expansion,  $\bar{D}^* \gg D^*$ . Thus, the 2s full complement subspace (obtained by excluding the 1s variational space from the 2s variational space), is likewise much larger than needed for energy minimization—only a small subspace thereof really matters. CBE aims to identify parts of that small subspace; shrewd selection offers a cheap way of doing so, yielding a notable speedup when computing the truncated complement.

## C. Singular vectors

We next turn to a comparison of singular vectors to further quantify the benefits of using (II) moderate rather than (III) severe preselection, and of using final selection.

For the latter purpose, we consider a truncation scheme (V) involving moderate preselection but no final selec-

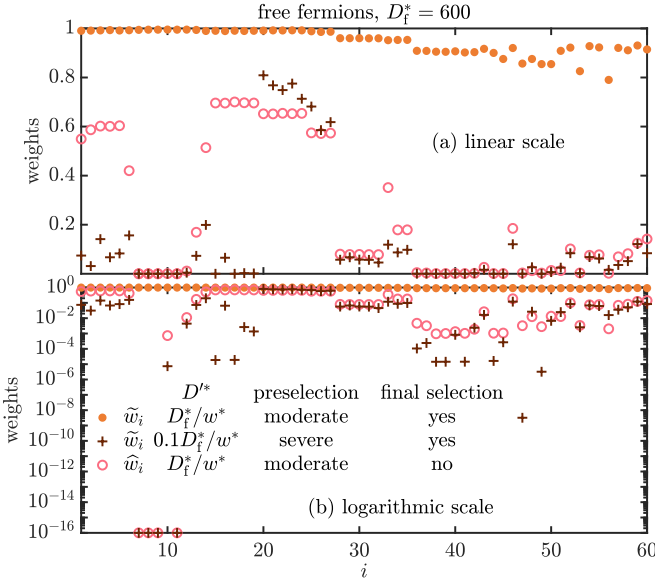


FIG. S-2. Comparison of weights (S3) with which reference singular vectors  $\bar{S}_i$  from  $\bar{A}_\ell^{\text{tr}}$  (yellow triangle) are supported in truncated spaces obtained with three truncation settings (II-IV) defined in Sec. S-1 A:  $\tilde{w}_i$  gives the weight of  $|\bar{S}_i\rangle$  in  $\text{span}\{|\bar{S}_j\rangle\}$ , the image of  $\bar{A}_\ell^{\text{tr}}$  (yellow triangle), computed through shrewd selection, using either (II) moderate (orange dots) or (III) severe (brown crosses) preselection; and  $\hat{w}_i$  gives the weight of  $|\bar{S}_i\rangle$  in  $\text{span}\{|\hat{S}_j\rangle\}$ , the image of  $\hat{A}_\ell^{\text{pr}}$  (pink triangle), computed using (IV) moderate preselection without final selection (pink circles). Both panels show the same data, on (a) a linear and (b) a log scale.

tion: after the minimization of the cost function  $\mathcal{C}_2$  (see Fig. 2(c)), we directly truncate  $\hat{U} \hat{S} \hat{V}^\dagger \simeq \hat{U} \hat{s} \hat{v}^\dagger$  from  $\hat{D}^*$  to  $\tilde{D}^*$ , and define the truncated complement as  $\hat{A}_\ell^{\text{tr}} = \hat{U}$  (pink triangle), with singular vectors  $|\hat{S}_i\rangle$ .

To compare singular vectors we compute the weights

$$\tilde{w}_i = \sum_{j=1}^{\tilde{D}^*} |\langle \bar{S}_j | \bar{S}_i \rangle|^2 = \begin{array}{c} \text{diag} \\ \text{yellow} \end{array}^i, \quad (\text{S3a})$$

$$\hat{w}_i = \sum_{j=1}^{\tilde{D}^*} |\langle \hat{S}_j | \bar{S}_i \rangle|^2 = \begin{array}{c} \text{diag} \\ \text{pink} \end{array}^i. \quad (\text{S3b})$$

Here,  $\tilde{w}_i$  is the weight with which a singular vector  $|\bar{S}_i\rangle$  (ordered by size of corresponding singular value) from the image of  $\bar{A}_\ell^{\text{tr}}$  (yellow triangle) is supported in the subspace  $\text{span}\{|\bar{S}_j\rangle\}$ , the image of  $\bar{A}_\ell^{\text{tr}}$  (yellow triangle); and  $\hat{w}_i$  gives its weight in  $\text{span}\{|\hat{S}_j\rangle\}$ , the image of  $\hat{A}_\ell^{\text{tr}}$  (pink triangle). In less technical terms, the weights characterize how well reference singular vectors can be represented in these truncated spaces.

These weights are shown in Fig. S-2 for the free fermion data corresponding to Fig. S-1(a). For (II) moderate preselection plus final selection ( $\tilde{w}_i$ , orange dots), all weights are close to one. Thus, this truncation scheme almost perfectly captures that part of the 2s subspace most relevant for minimizing the GS energy. By contrast, for both (III)

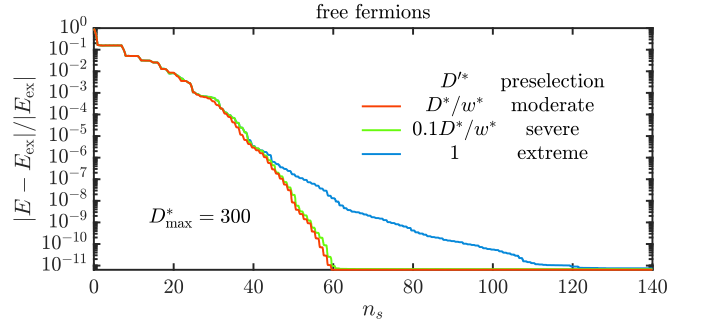


FIG. S-3. Influence of preselection on CBE-DMRG convergence rate, for a half-filled free-fermion chain ( $\mathcal{L} = N = 20$ ). The GS energy is plotted as function of the number of half-sweeps,  $n_s$ , for three values of  $D'^*$ , used for preselection. We start from a  $D_i^* = 1$  valence bond state, set  $\delta = 0.1$ , increase  $D^*$  using  $\alpha = 1.1$  until  $D^* = 300$  is reached, and continue sweeping with  $\alpha = 1$  thereafter.

severe preselection plus final selection ( $\tilde{w}_i$ , brown crosses) and (V) moderate preselection without final selection ( $\hat{w}_i$ , pink circles), most weights are significantly smaller than 1; four are numerically zero. Thus, both these schemes discard a significant part of the space relevant for minimizing the GS energy.

#### D. Convergence rate per sweep

The weights obtained for severe preselection ( $D'^* = \delta D^*/w^*$ ) in Fig. S-2 pose the question whether  $D'^*$  can be too small to give converged results. In this case, preselection would not only be inefficient, but actually unsuccessful. To explore this, Fig. S-3 compares the CBE-DMRG convergence rate for several choices of  $D'^*$ , corresponding to (II) moderate (red), (III) severe (green), and (IV) extreme (blue) preselection.

As expected, convergence slows down with smaller  $D'^*$ . Remarkably, however, once convergence has been reached, the converged results agree (even for  $D'^* = 1$ , a truly extreme choice!). In this sense, the preselection strategy is robust—converged results don't depend on  $D'^*$ . Note, though, that the computation time does not depend significantly on  $D'^*$  (provided it is clearly smaller than  $D^*$ ). On the other hand, it obviously does depend on the number of sweeps, and the time per sweep can be very large for expensive models. Therefore,  $D'^*$  should not be chosen too small, to avoid a time-costly increase in the number of sweeps.

To summarize: a bond expansion is *efficient*, yielding a significant reduction in GS energy and therefore quick convergence, if  $D'^*$  is large enough that the “most important” states  $|\bar{S}_i\rangle$ , i.e. those with the largest singular values  $\bar{S}_i$ , are well represented in the expanded space, i.e. have weights  $\tilde{w}_i \simeq 1$ .

However, even if  $D'^*$  is so small that most of the im-

portant states  $|\bar{s}_i\rangle$  are represented with small weights, a bond expansion can nevertheless be *successful*, in the sense of adding some relevant new states, provided that these weights are non-zero,  $\tilde{w}_i \neq 0$ . The reason is that the states  $|\tilde{s}_i\rangle$  added to  $A_\ell(\nabla)$  contain information about the optimal states  $|\bar{s}_i\rangle$  with finite  $\tilde{w}_i$ , i.e. those  $|\bar{s}_i\rangle$  are not orthogonal to the expanded kept space. As long as this information is available, subsequent 1s updates will optimize the kept sector accordingly; the states  $|\tilde{s}_i\rangle$  just offer a somewhat less optimal starting point for that than the  $|\bar{s}_i\rangle$ .

Note that it is of utmost importance for successful bond expansion that information on the *most important*  $|\bar{s}_i\rangle$  is included. Since only a small set of states is in the end used for expansion, the most important states must be prioritized; otherwise, inferior information is included in the kept space, rendering the bond expansion unsuccessful: Subsequent 1s updates may then optimize towards a suboptimal kept sector, as the optimal one may not be available to the 1s update, e.g. due to symmetry constraints. The energy will still decrease due to the unsuccessful bond expansion plus 1s update, but not as much as if the correct information on the most important  $|\bar{s}_i\rangle$  is correctly included. The result will be a suboptimal final state at the desired finite bond dimension  $D_{\max}^*$ , i.e. we have wasted resources.

Fig. S-3 shows that CBE-DMRG correctly includes information on the most optimal states when expanding the bond, independent of  $D'^*$ . Even with extreme preselection ( $D'^* = 1$ ), it does not get stuck with some sub-optimal state at  $D_{\max}^* = 300$ , but eventually converges (albeit slowly) to the same GS as found with larger choices of  $D_{\max}$ .

## S-2. FERMIONIC MODELS ON CYLINDERS

In this section, we show that our CBE-DMRG methods works well also for rather challenging fermionic models on  $10 \times 4$  cylinders. We first show that for the Hubbard model on a  $10 \times 4$  cylinder, we obtain results in line with Ref. 26. Then, we show results for a Kondo-Heisenberg-Holstein (KHH) model on a  $10 \times 4$  cylinder, featuring huge physical and MPO bond dimensions up to  $d^*[d]=16[32]$  and  $w^*[w]=14[30]$ , respectively. Our intention is to show that CBE-DMRG is stable for models at the edge of what is possible with current DMRG techniques, not to discuss their rich physics.

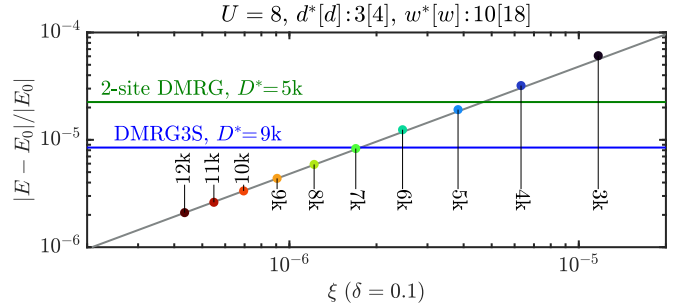


FIG. S-4. Error in GS energy versus discarded weight for the Hubbard model on a  $10 \times 4$  cylinder. The reference energy  $E_0 = -27.8816942$  is obtained by linear  $\xi$ -extrapolation to  $\xi=0$  (grey line) using the largest four  $D^*$  values.  $D^*$  values are shown next to their corresponding data point. The horizontal lines show the most accurate computations with 2s DMRG and DMRG3S from Ref. 26, table I as reference values.

### A. Hubbard model

The Hubbard model on a  $10 \times 4$  cylinder is described by the Hamiltonian

$$H_{\text{H}} = - \sum_{\sigma=\uparrow,\downarrow} \sum_{\langle \ell, \ell' \rangle} \left( c_{\ell\sigma}^\dagger c_{\ell'\sigma} + h.c. \right) + U \sum_{\ell} n_{\ell\uparrow} n_{\ell\downarrow}. \quad (\text{S4})$$

where  $\ell = (x, y)$  is a 2D site index,  $\sum_{\langle \ell, \ell' \rangle}$  a sum over nearest-neighbors,  $c_{\ell\sigma}^\dagger$  are fermionic creation operators at site  $\ell$  with spin  $\sigma$  and  $n_{\ell\sigma} = c_{\ell\sigma}^\dagger c_{\ell\sigma}$  are the corresponding number operators. Following Ref. 26, we choose  $U = 8$ , and search for the GS in the sector with total filling  $N = 36$ , i.e. 10% hole doping, and total spin  $S = 0$ . We exploit  $U(1)_{\text{ch}} \otimes SU(2)_{\text{sp}}$  charge and spin symmetries. The MPO is implemented in real space, snaking around the cylinder (in contrast to Ref. 26, where a hybrid-space implementation was used).

Our CBE-DMRG results, shown in Fig. S-4 show nice convergence with  $D^*$ , indicated by the linear  $\xi$  scaling of the energy. We obtain comparable GS energies as in Ref. 26, but for given  $D^*$  reach slightly lower energies. We attribute this difference to the different MPO implementations used (real-space vs. hybrid-space)[13, 39].

### B. Kondo-Heisenberg-Holstein model

As an even more challenging application of CBE-DMRG, we compute the GS of a Kondo-Heisenberg-Holstein (KHH) model on a  $10 \times 4$  cylinder.

The KHH model consists of conduction electron, local magnetic moment and Holstein-phonon degrees of freedom, described by the Hamiltonian

$$H_{\text{KHH}} = - \sum_{\sigma=\uparrow,\downarrow} \sum_{\langle \ell, \ell' \rangle} (c_{\ell\sigma}^\dagger c_{\ell'\sigma} + h.c.) \quad (\text{S5})$$

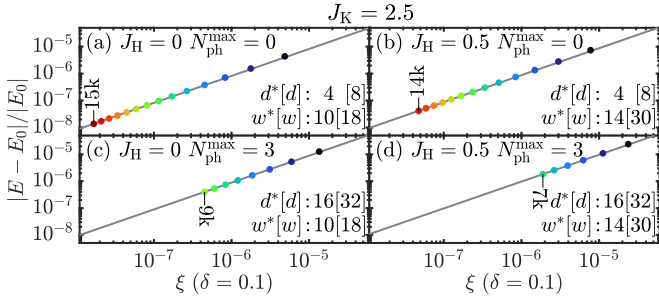


FIG. S-5. Error in GS energy versus discarded weight for the KHH model on a  $10 \times 4$  cylinder, with (a) only Kondo coupling, (b) Kondo and Heisenberg coupling, (c) Kondo and Holstein coupling and (c) Kondo, Heisenberg and Holstein coupling. Legends state our choices for  $J_H$  and  $N_{ph}^{max}$ , and corresponding values of  $d^*[d]$  and  $w^*[w]$ . For each panel,  $E_0$  was obtained by linear  $\xi$ -extrapolation to  $\xi = 0$  (grey line) using the four largest  $D^*$  values. The very largest  $D^*$  is shown next to its data point;  $D^*$  changes by 1k between adjacent data points.

$$+ 2J_K \sum_{\ell} \mathbf{S}_{\ell} \cdot \mathbf{s}_{\ell} + J_H \sum_{\langle \ell, \ell' \rangle} \mathbf{S}_{\ell} \cdot \mathbf{S}_{\ell'} \\ + \omega_{ph} \sum_{\ell} b_{\ell}^{\dagger} b_{\ell} + g \sum_{\ell} (n_{\ell\uparrow} + n_{\ell\downarrow} - 1)(b_{\ell}^{\dagger} + b_{\ell}).$$

We use the same notation for fermion operators  $c_{\ell\sigma}^{\dagger}$  on a cylinder as in Eq. (S4) for the Hubbard model. Moreover,  $\mathbf{s}_{\ell} = \frac{1}{2} \sum_{ss'} c_{\ell s}^{\dagger} \boldsymbol{\sigma}_{ss'} c_{\ell s'}$  is the conduction electron spin operator,  $\mathbf{S}_{\ell}$  the spin operator of a spin  $\frac{1}{2}$  local moment, and  $b_{\ell}^{\dagger}$  a phonon creation operator, all for site  $\ell$ .

To deal with the infinite local phonon Hilbert space, we restrict the maximum number of local phonon excitations to  $N_{ph}^{max}$  (specified below) in our DMRG calculations.

The KHH model is relevant for heavy-fermion materials, which consist of itinerant conduction electrons, hybridiz-

ing with localized  $f$  orbitals [40]. At low energies, only the spin degree of freedom of the  $f$  electrons remain, leading to a Kondo-Heisenberg (KH) model, which is the KHH model at  $N_{ph}^{max} = 0$ . While the inclusion of optical phonon degrees of freedom, which leads to the KHH model, is rather scarce in the literature, there is experimental data available suggesting these may play a role in heavy-fermion physics [41].

Heavy-fermion materials feature many interesting phenomena. One of the not so well understood ones is the so-called Kondo breakdown quantum critical point. When the system is tuned across this critical point, the FS volume abruptly changes [42], leading to a violation of Luttinger's theorem [43] and strange metal behavior at finite temperatures. Here, our goal is just to showcase the ability of CBE-DMRG to deal with the KHH model; we leave the discussion of its rich physics to future work.

In our CBE-DMRG calculations, we use Kondo-coupling  $J_K = 2.5$ , Holstein-coupling  $g = 0.5$  to the phonons and optical phonon frequency  $\omega_{ph} = 0.5$ . Two different values for  $N_{ph}^{max} \in \{0, 3\}$  and the Heisenberg coupling  $J_H \in \{0, 0.5\}$  are considered, respectively.

We performed GS searches for  $N = \mathcal{L}(1 + \frac{1}{4}) = 50$  and  $S = 0$ , i.e. at 25% electron doping. Figure S-5 shows the energy error vs.  $\xi$  for four parameter combinations (see legends). The linear  $\xi$ -dependence of  $E$  demonstrates proper convergence of CBE-DMRG. Very large  $D^*$  values are achievable despite the rather huge values of  $d$  and  $w$ . This is remarkable especially for  $J_H = 0.5$  and  $N_{ph}^{max} = 3$  (Fig. S-5(d)), where 2s schemes become excessively costly.

### S-3. PSEUDOCODE FOR SHREWD SELECTION

Below, we provide a pseudocode for computing the truncated complement during CBE using shrewd selection.

---

**Algorithm 1** Computation of truncated complement using shrewd selection

---

**Input:** 2s Hamiltonian  $H_\ell^{2s} = L_{\ell-1}W_\ell W_{\ell+1}R_{\ell+2}$ , 2s wavefunction  $\psi^{2s} = A_\ell \Lambda_\ell B_{\ell+1}$  in bond-canonical form, preselection bond-dimension  $D'$ , truncated complement dimension  $\tilde{D}$

**Output:** truncated complement  $\tilde{A}_\ell^{\text{tr}}$  (▽)

- 1: **function** GETRORTH( $R_{\ell+2}, W_{\ell+1}, B_{\ell+1}, \Lambda_\ell$ )
- 2:   Compute  $R_{\ell+1}^{\text{tmp}} = \Lambda_\ell B_{\ell+1} W_{\ell+1} R_{\ell+2}$
- 3:   Compute  $R_{\ell+1}^{\text{orth}} = R_{\ell+1}^{\text{tmp}} - R_{\ell+1}^{\text{tmp}} B_{\ell+1}^\dagger B_{\ell+1}$
- 4:   **return**  $R_{\ell+1}^{\text{orth}}$
- 5: **end function**
- 6: (Fig. 2(a)): SVD  $\ell$ -bond of  $R_{\ell+1}^{\text{orth}} = USV^\dagger$
- 7: **function** GETLORTH( $L_{\ell-1}, W_\ell, A_\ell, U, S$ )
- 8:   Compute  $L_\ell^{\text{tmp}} = L_{\ell-1} W_\ell U S$
- 9:   Compute  $L_\ell^{\text{orth}} = L_\ell^{\text{tmp}} - A_\ell A_\ell^\dagger L_\ell^{\text{tmp}}$
- 10:   **return**  $L_\ell^{\text{orth}}$
- 11: **end function**
- 12: (Fig. 2(b)): SVD  $L_\ell^{\text{orth}} = U' S' V'^\dagger$  and truncate all except the largest  $D'$  singular values in  $S'$ :  $U' S' V'^\dagger \xrightarrow{\text{trunc}} u' s' v'^\dagger$
- 13: (Fig. 2(c)): Redirect the MPO-leg of  $u' s'$  and perform an SVD on its combined MPO- and  $\ell$ -bond,  $u' s' = \hat{U} \hat{S} \hat{V}^\dagger$ . Truncate all singular values in  $\hat{S}$  which are numerically zero to ensure  $A_\ell^\dagger \hat{U} = 0$ . ▷ **warning:**  $A_\ell^\dagger \hat{U} = 0$  is crucial and *must* be ensured!
- 14: (Optional): safety orthogonalization of  $\hat{U}$  by SVD on  $\hat{U} - A_\ell A_\ell^\dagger \hat{U}$  plus truncation of small singular values.
- 15: Assign  $\hat{A}_\ell^{\text{pr}} = \hat{U}$  (▽)
- 16: **function** GETCORTH( $L_{\ell-1}, W_\ell, W_{\ell+1}, R_{\ell+2}, A_\ell, \Lambda_\ell, B_{\ell+1}, \hat{A}_\ell^{\text{pr}}$ )
- 17:   Compute  $L_\ell^{\text{pr}} = (\hat{A}_\ell^{\text{pr}})^\dagger L_{\ell-1} W_\ell A_\ell$
- 18:   Compute  $C_{\ell+1}^{\text{tmp}} = L_\ell^{\text{pr}} \Lambda_\ell B_{\ell+1} W_{\ell+1} R_{\ell+2}$
- 19:   Compute  $C_{\ell+1}^{\text{orth}} = C_{\ell+1}^{\text{tmp}} - C_{\ell+1}^{\text{tmp}} B_{\ell+1}^\dagger B_{\ell+1}$
- 20:   **return**  $C_{\ell+1}^{\text{orth}}$
- 21: **end function**
- 22: (Fig. 2(d)): SVD  $C_{\ell+1}^{\text{orth}} = \tilde{U} \tilde{S} \tilde{V}^\dagger$  and truncate all except the largest  $\tilde{D}$  singular values:  $\tilde{U} \tilde{S} \tilde{V}^\dagger \xrightarrow{\text{trunc}} \tilde{u} \tilde{s} \tilde{v}^\dagger$
- 23: Compute  $\tilde{A}_\ell^{\text{tr}} = \hat{A}_\ell^{\text{pr}} \tilde{u}$  (▽)

---

TABLE I. Pseudocode for computing the truncated complement  $\tilde{A}_\ell^{\text{tr}}$  using shrewd selection.